Wind Vibration Analyses of Giant Magellan Telescope

Frank W. Kan* and Daniel W. Eggers
Simpson Gumpertz & Heger Inc.
41 Seyon Street, Building 1, Suite 500, Waltham, MA 02453 USA

ABSTRACT

The Giant Magellan Telescope (GMT) will be a 21.5-m equivalent aperture optical-infrared telescope located in Chile. The segmented mirror surface consists of seven 8.4-m diameter mirrors. The telescope structure will be inside a carousel-type enclosure. This paper describes the wind vibration analyses performed on the baseline configuration of the GMT structure during the conceptual design phase. The purposes of the study were to determine order of magnitude pointing and focus errors resulting from the dynamic response of the telescope structure to wind disturbances, and to identify possible changes to the structure to reduce the optical errors. In this study, wind pressure and velocity data recorded at the 8-m Gemini South Telescope were used to estimate the dynamic wind load on the GMT structure. Random response analyses were performed on a finite element model of the telescope structure to determine the structural response to dynamic wind loading and the resulting optical errors. Several areas that significantly contribute to the optical errors were identified using the spectral response curves and the mode shapes. Modifications to these areas were developed and analyzed to determine their effects on the optical performance, and an improved design was developed for the next phase of the design.

Keywords: Wind vibration, dynamic response, optical performance, finite element analysis

1. INTRODUCTION

The Giant Magellan Telescope (GMT) shown in Fig. 1 is to be a 21.5-m equivalent aperture optical-infrared telescope located in Chile. The segmented mirror surface consists of seven 8.4-m diameter borosilicate honeycomb mirrors. Each primary mirror is supported on hydraulic mounts connected to a mirror-cell structure. The cell-connector frame supports all seven mirror cells and the secondary truss at three bracket locations. The C-ring assembly supports the cell-connector frame, houses and supports the instrument platform, and defines the altitude axis via hydrostatic bearings. The azimuth structure consists of a large azimuth disk and four OSS support pedestals. The entire structure is supported by the azimuth track and pier, and is housed within a carousel-type enclosure. The details of the telescope structure were presented by Gunnels et al. [1].

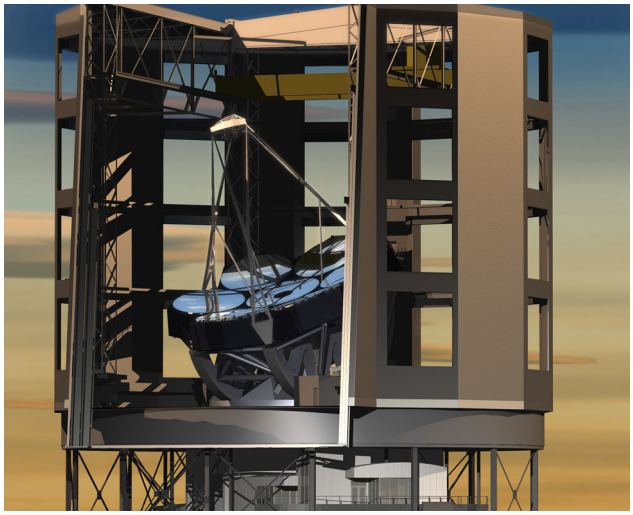

Fig. 1 – Artist's rendering of Giant Magellan Telescope in its enclosure [2]

This paper describes the wind vibration analyses performed on the baseline configuration of the GMT structure during the conceptual design phase. The purposes of the study are (1) to study the dynamic response of the GMT structure to wind disturbance with the goal of determining order of magnitude pointing and focus errors, and (2) to identify possible changes to the structure to improve the pointing accuracy.

*fwkan@sgh.com; phone 1 781 907-9233; fax 1 781 907-9009; http://www.sgh.com

In this study, wind pressure and velocity data recorded at the 8-m Gemini South Telescope were used to estimate the dynamic wind load on the GMT structure. Random response analyses were performed on a finite element model of the baseline configuration of the telescope structure to determine the structural response to dynamic wind loading and the resulting optical errors. Several areas that significantly contribute to the optical errors were identified using the spectral response curves and the mode shapes. Modifications to these areas were developed and analyzed to determine their effects on the optical performance, and an improved design was developed for the next phase of the design.

2. FINITE ELEMENT MODEL

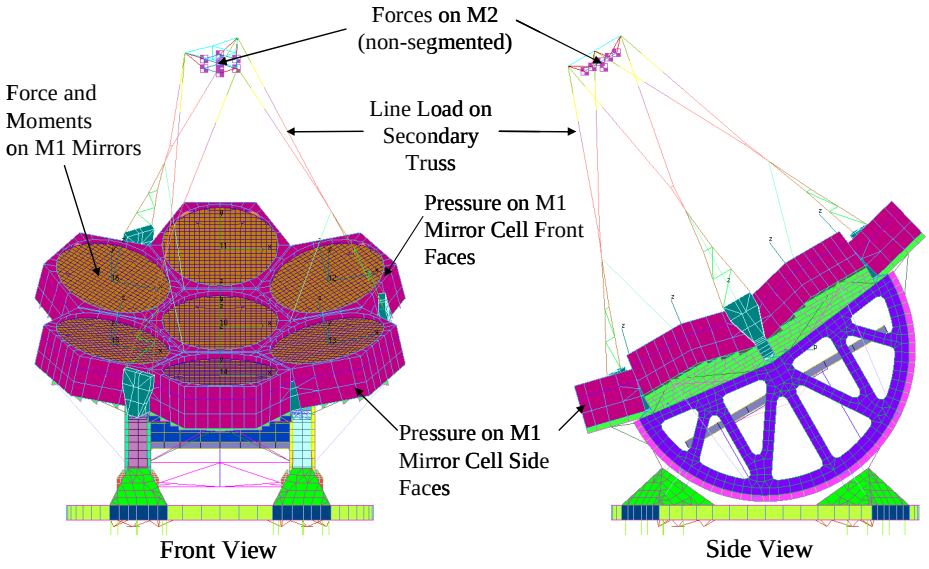

Fig. 2 – Finite element model of baseline design of GMT telescope structure at 30° zenith angle

The finite element model used in this study originated from the ALGOR models [1] developed by Mr. Steve Gunnels of Paragon Engineering and was converted into MSC/NASTRAN (Fig. 2).

In the FEM, the primary mirror segments, the primary mirror cells, the cell-connector frame, the C-ring structures, the instrument platform, the azimuth disk, and the OSS pedestals are modeled by plate elements. The hexapod mirror support, the secondary truss, the secondary support structure, and all the braces are modeled by beam elements. The weights of the secondary mirrors and their mirror cells are included as lumped masses. The stiffnesses of the hydrostatic bearings and of the telescope drives are modeled by equivalent beam elements.

The authors modified the FEM to include wind loads on the primary mirror segments, primary mirror cells, secondary truss, secondary support structure, secondary mirror, and secondary mirror cell (Fig. 2). The details of the wind loads are discussed in the next section.

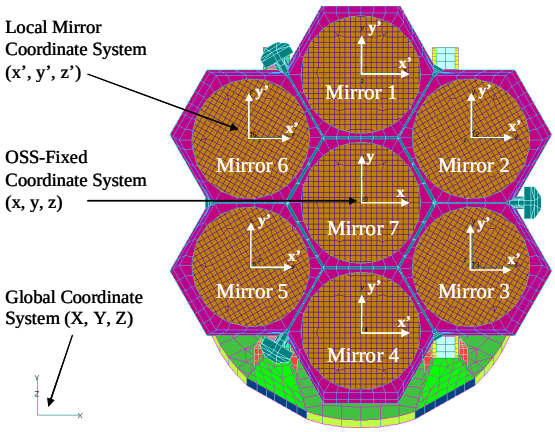

Fig. 3 – View of FEM from M2 towards M1 showing mirror numbering and coordinate system (Secondary Truss and M2 not shown for clarity)

Additional nodes, interpolation elements, and constraint equations were added to the FEM to calculate the pointing and focus errors directly from the analyses (see Section 4).

The primary mirrors are numbered from 1 to 6 clockwise starting at 12:00 and the center mirror is No. 7 (Fig. 3). Fig. 3 also shows the three coordinate systems used in the FEM. The local mirror coordinate systems (x', y', z'), the OSS-

fixed coordinate system (x, y, z), and the global coordinate system (X, Y, Z) are Cartesian coordinates fixed to the undeformed physical structure or to the ground.

3. DYNAMIC WIND LOAD

This section presents the wind measurement data and the methodology used in the development of the dynamic wind loads applied to different parts of the telescope structure in the wind vibration analyses.

Dynamic wind loads can be treated as random excitations that can be described only in a statistical sense. The instantaneous magnitude is not known at any given time; rather, the magnitude is expressed in terms of its statistical properties (such as mean value, standard deviation, and probability of exceeding a certain value). The random excitations are usually described in terms of power spectral density (PSD) functions.

3.1 Wind Data

The dynamic wind data used in this study are based on actual pressure and velocity measurements taken by Gemini Observatory during the integration of Gemini South Telescope atop Chile's Cerro Pachón [3]. The Gemini South Telescope has a single 8-m optical mirror within an enclosure shown in Fig. 4.

Vent Gates Closed Vent Gates Open

Fig. 4- Gemini South Telescope enclosure [4]

The test on Gemini South Telescope included twenty-four wind pressure measurements and five wind speed measurements for different wind directions (azimuth angle of attack), telescope orientations (zenith angles), upwind vent-gate positions, downwind vent-gate positions, and wind screen positions. The twenty-four pressure transducers were mounted on the dummy 8-m mirror cell over a 1.4 m by 1.4 m grid. Five three-axis ultrasonic anemometers were used to measure the wind speeds at the top of the enclosure, at the secondary mirror, and at the edge of the primary mirror at 3:00, 6:00, and 9:00 locations. All the records were 300 sec in length and were sampled at 10 Hz. Some pressure transducer measurements were also recorded on another system and were sampled at 200 Hz. The power spectral density and time history data are available on the AURA New Initiatives Office website [4].

The following two cases were chosen for study since they are real configurations which might occur during an observation:

- Case 1 – Vent gate open, wind screen open, telescope pointing into wind, and zenith angle = 30°.
- Case 2 – Vent gate closed, wind screen closed, telescope pointing into wind, and zenith angle = 30°.

In both cases, the average outside wind speed was about 13 m/sec. At Las Campanas Observatory, this represents the 90^{th}-95^{th} percentile wind speed depending on the site.

Since most of the Gemini South wind measurements were sampled at a rate of 10 Hz, the resulting PSD curves need to be extrapolated beyond 5 Hz. Examination of some of the data shows that the PSD curves for Case 2 do not roll off as quickly as those for Case 1. Measurements sampled at 200 Hz were examined. Fig. 5 shows the pressure PSD of Pressure Tap 1 with 10 Hz and 200 Hz sampling rate for Cases 1 and 2. For Case 1, the data with 200 Hz sampling rate clearly shows a constant slope roll-off in the log-log scale beyond 5 Hz. For Case 2, both data sets appear to encounter a noise floor at the higher frequencies. The data with 200 Hz sampling rate shows a constant slope roll-off in the log-log scale from 1 to 5 Hz similar to that of Case 1. However, the data with 10 Hz sampling rate deviates from the 200 Hz data beyond 1 Hz. The actual spectra are expected to have a constant slope roll-off on the log-log

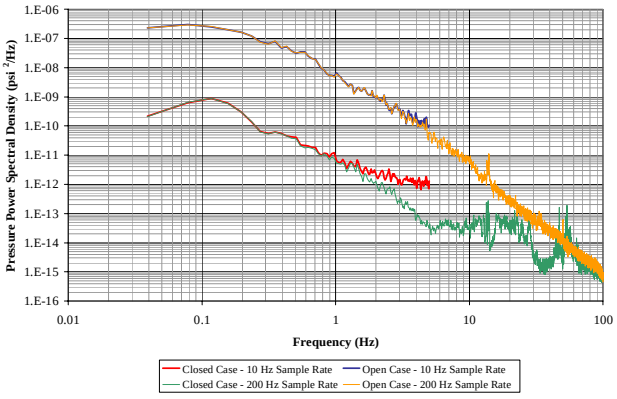

Fig. 5 – Wind pressure PSD at pressure tap 1 for Cases 1 and 2 with 10 Hz and 200 Hz sampling rate

scale for Case 2 as well, and the discrepancies are probably results of limitations on measurement at low pressures.

3.2 Wind Loads on Telescope Structure

The pressure and velocity measurements described in the above section were used to develop the dynamic wind load spectra on different parts of the telescope structure. Wind loads were applied to the following areas: (1) primary mirror surfaces, (2) primary mirror cells, (3) secondary truss and secondary support structure, and (4) secondary mirror and secondary mirror cell. No wind load was applied to the back face of the primary mirror cells, the C-ring structure, the instrument platform, or other braces below the mirror surface. These areas were assumed to be shielded.

The basic methodology is to apply the wind loads in form of pressure, line load, and concentrated force/moment spectra to plate element, beam elements, and nodes, respectively. Loads are applied over regions consisting of elements or nodes. Loads within each region are assumed to be fully correlated, and loads from different regions are assumed to be uncorrelated.

To convert the velocity measurement into pressure PSD, the velocity time history measurements were squared and the velocity squared PSD's were calculated. The air density for an altitude of 9,000 ft was used in the calculation of the pressure PSD's from the velocity squared PSD's.

In the following sections, the wind loads applied to different parts of the telescope are discussed in details.

3.2.1 Primary Mirror Surfaces

Random excitation force and moment resultants were applied to each of the seven primary mirrors. The power spectral densities of the force and moment resultants were computed based actual pressure measurements recorded on the M1 mirror at Gemini South. The force and moment time histories were calculated using the time histories of the twenty-four pressure taps and the tributary area of each pressure tap. The calculation assumes fully correlated pressure over the tributary area of a pressure tap. This methodology fully preserves all relevant time history pressure correlations over the surface of the mirror.

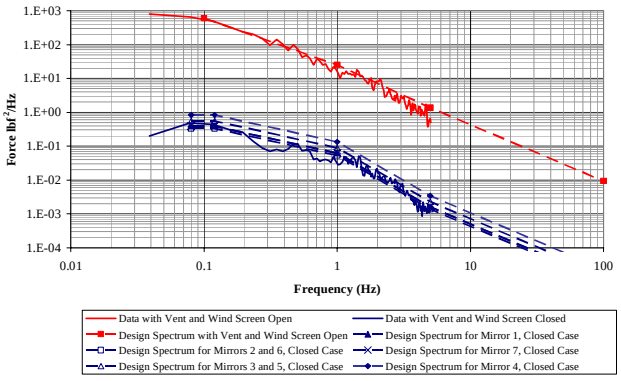

Fig. 6 – PSD of M1 force for Cases 1 & 2

The power spectral densities of the force and moment resultants scaled to the size of the GMT mirror (8.4 m) are shown in Figs. 6 through 8 for Cases 1 and 2.

For Case 1 (vent gates open and wind screen open), there is little or no correlation among the force, moment about x-axis, and moment about y-axis. The force and moment resultants were applied as uncorrelated nodal forces and moments at the center of each mirror in its local mirror coordinate system. The resultants were distributed to all of the nodes of each mirror via a RBE3 interpolation element.

For Case 2 (vent gates closed and wind screen closed), there is a correlation between the force and moment about x-axis due to uneven pressure distribution on the mirror face mainly along the y-direction.

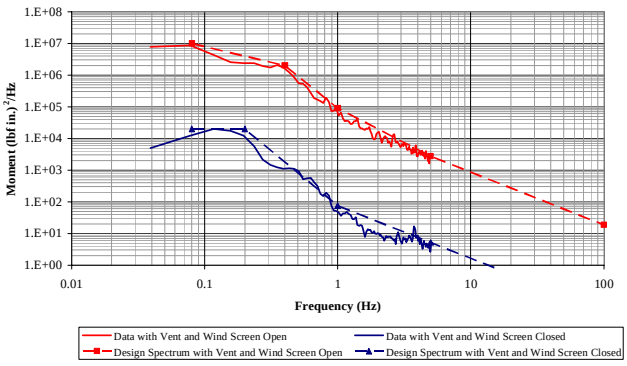

Fig. 7 – PSD of M1 moment about x-axis for Cases 1 & 2

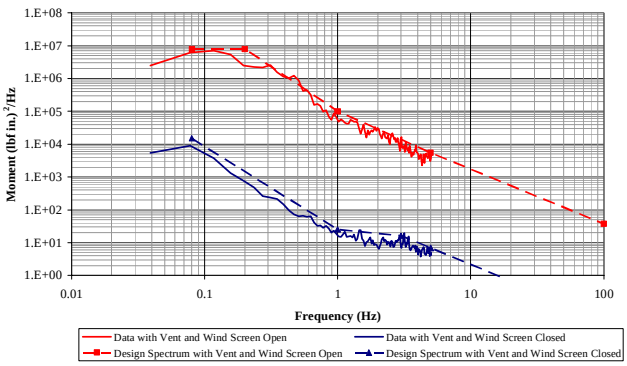

Fig. 8 – PSD of M1 moment about y-axis for Cases 1 & 2

This may be in part due to the configuration of the wind screen resulting in a wind gradient on the mirror surface. To account for this gradient, the calculated moment resultants to each of the seven mirrors were applied and the calculated force resultants for each mirror were scaled by the best fit line to the normalized cumulative energy of each pressure tap contained between 0.2 Hz and 2 Hz and the elevation of each tap. The scaled force resultant PSD curves for the seven mirrors are shown in Fig. 6.

An alternative method to apply the wind pressure on the primary mirrors was also investigated. In this method, each mirror was divided into a number of zones over which pressure was assumed to be correlated. Wind pressures of adjacent regions were assumed to be uncorrelated. The average of the wind pressure PSD recorded on Gemini South M1 mirror was used for all regions. A nine region (3 x 3) layout on each mirror segment was used in this study.

3.2.2 Primary Mirror Cells

Random excitation pressures were applied to the front edges and side faces of the primary mirror cells. For the front edges, the average of the wind pressure PSD recorded on the Gemini South M1 mirror was used. Six edge regions per cell were used. For the side faces, a reference pressure PSD was calculated based on the average of the velocity squared PSD recorded by three anemometers above the edges of the Gemini South M1 mirror cell. The reference pressure was multiplied by a pressure coefficient to account for the shape of the mirror cell and the orientation of the face. The pressure coefficients around a short cylinder given in Ref. [5] were used. Each primary mirror cell was considered to be a separate cylinder assuming no interaction between adjacent mirror cells. Pressures were applied to the exposed side faces of the six outer mirror cells with each face as a region for a total of eighteen regions.

3.2.3 Secondary Truss and Secondary Support Structure

Distributed loads were applied to the secondary truss and the secondary support structure. A reference pressure PSD was calculated based on the average of the velocity squared PSD recorded by the anemometer located just above the Gemini South M2 mirror. A velocity factor of 1.17 was used to account for possible increase in wind velocity due to the increased height of the GMT relative to the Gemini South Telescope. The reference pressure was multiplied by a drag coefficient to account for the shape and orientation of the member. The drag coefficients in Ref. [5] were used. Distributed loads were applied in four separate regions along each of the six legs of the secondary truss. Distributed loads were also applied to each of the crossover braces and diagonal braces as separate regions. The secondary support structure was divided into three separate regions with distributed loads applied to the members.

3.2.4 Secondary Mirror and Secondary Mirror Cell

Nodal forces were applied to the seven M2 mirrors and their mirror cells. The same reference pressure PSD described in the previous section was used. The force on each of the seven mirror cells was computed and applied as concentrated forces at the C.G. of each mirror-cell assembly. The forces on the seven M2 mirrors were assumed to be correlated. A sensitivity analysis was also performed with uncorrelated forces on the seven M2 mirrors.

4. OPTICAL SENSITIVITY EQUATIONS

Optical sensitivity equations were used to calculate the pointing and focus errors resulting from displacements and rotations of the optical components of the telescope, namely the seven primary mirror (M1) segments, the secondary mirrors (M2), and the instrument platform (IP). These equations were developed by Dr. Matthew Johns of Carnegie Observatories [6] and were included in the finite element model as constraint equations.

For each primary mirror segment, a target node is defined on the telescope optical axis at the vertex of the parent conic surface. The average displacements and rotations of each mirror segment at its target node are computed using a RBE3 interpolation element. The secondary mirrors are assumed to behave as a single mirror; therefore, the rigid body displacements and rotations at its vertex are used. For the instrument platform, the translations of the target node located at the nominal focus position are used.

The x and y-pointing errors and z-focus error of each primary mirror segment were calculated using constraint equations in the finite element model. The weighted means of these errors were also calculated using constraint equations.

4.1 Pointing Error

The x and y-motions (mm) of the line of sight referenced to the unperturbed focal plane for each of the seven subapertures of the telescope are given by:

$$\Delta_x^{(i)} = (-11.26) * x_1^{(i)} + (-1.966) * \Theta_{y,1}^{(i)} + (12.26) * x_2 + (-0.250) * \Theta_{y,2} + (-1.00) * x_3 \quad (1)$$

$$\Delta_y^{(i)} = (-11.26) * y_1^{(i)} - (-1.966) * \Theta_{x,1}^{(i)} + (12.26) * y_2 - (-0.250) * \Theta_{x,2} + (-1.00) * y_3 \quad (2)$$

where i = 1 to 6 refer to the off-axis primary mirror segments and i = 7 refers to the center primary mirror segment and:

- $x_1^{(i)}$ and $y_1^{(i)}$ are the x and y-displacements (mm) of the target node representing the i^{th} primary mirror segment
- $\Theta_{x,1}^{(i)}$ and $\Theta_{y,1}^{(i)}$ are the rotations (arcsec) of the target node representing the i^{th} primary mirror segment about the x and y-axes
- x_2 and y_2 are the x and y-displacements (mm) of the secondary mirror
- $\Theta_{x,2}$ and $\Theta_{y,2}$ are the rotations (arcsec) of the secondary mirror about the x and y-axes
- x_3 and y_3 are the x and y-displacements (mm) of the instrument platform

The mean x and y-displacements weighted by mirror collecting areas are calculated as:

$$\Delta_x = 0.1465 * \sum_{i=1}^{6} \Delta_x^{(i)} + 0.1210 * \Delta_x^{(7)} \quad (3)$$

$$\Delta_y = 0.1465 * \sum_{i=1}^{6} \Delta_y^{(i)} + 0.1210 * \Delta_y^{(7)} \quad (4)$$

The values Δ_x and Δ_y may be converted to arcsec of image displacement by multiplying the displacement by the scale factor of 1.017 arcsec per millimeter (or 25.832 arcsec per inch).

4.2 Focus Error

The focus shift referenced to the unperturbed focal plane for each of the seven subapertures of the telescope is given by:

$$\Delta_z^{(i)} = (-127) * z_1^{(i)} + (128) * z_2 + (-1.00) * z_3 \quad (5)$$

where i = 1 to 6 refer to the off-axis primary mirror segments and i = 7 refers to the center primary mirror segment and:

- $z_1^{(i)}$ is the z-displacement (mm) of the target node representing the i^{th} primary mirror segment
- z_2 is the z-displacement (mm) of the secondary mirror
- z_3 is the z-displacement (mm) of the instrument platform

The mean focus shift weighted by mirror collecting areas is

$$\Delta_z = 0.1465 * \sum_{i=1}^{6} \Delta_z^{(i)} + 0.1210 * \Delta_z^{(7)} \quad (6)$$

5. RANDOM RESPONSE ANALYSES

Random vibration analyses were performed to obtain wind response of the structure using the finite element model with the wind loads and the optical sensitivity equations described in the previous sections.

The following three conditions were analyzed for the baseline configuration:

- Locked rotor with 2% damping and Case 1 (vent gates open and wind screen open)
- Locked rotor with 2% damping and Case 2 (vent gates closed and wind screen closed)
- Locked rotor with 0.5% damping and Case 1 (vent gates open and wind screen open)

A series of analyses were performed to investigate different stiffening options for the secondary truss. For these analyses, only the following condition was used:

- Locked rotor with 2% damping and Case 1 (vent gates open and wind screen open)

After the stiffening options for the secondary truss were selected, the same three conditions were repeated for the recommended configuration.

The effects of the correlation of the forces on the M2 mirrors were investigated using the baseline configuration. The effects of the different methods of applying wind loads on the M1 mirrors were investigated using one of the secondary truss stiffening options.

In all the analyses, the modes between 0 and 30 Hz were used. The responses were calculated over a frequency range of 0.1 – 25 Hz. The power spectral density (PSD) curves and RMS values of the following responses were calculated:

- Displacements and rotations of the seven M1 mirrors projected to the center of the primary conic surface
- Displacements and rotations of the M2 mirror, and instrument platform
- Pointing and focus errors

6. RESULTS OF ANALYSES

6.1 Results for Baseline Configuration

Eigenvalue analysis and random response analyses were performed for the baseline configuration. Table 1 lists the natural frequencies and mode shapes with locked-rotor condition.

Table 1 – Natural frequencies and mode shapes of baseline configuration

Mode	Frequency (Hz)	Mode Shape
1	4.43	Lateral Translation
2	5.40	Fore-Aft Translation
3	5.59	Azimuth Rotation
4	6.83	Secondary Truss Fore-Aft + Instrument Platform
5	7.17	Secondary Truss Lateral
6	7.41	Secondary Truss Fore-Aft
7	7.96	Secondary Truss Torsion
8	8.01	Secondary Truss Lateral

In addition to the natural frequencies and mode shapes listed above, there are many primary mirror modes with natural frequencies from 11.0 Hz to 12.5 Hz and many primary mirror-cell outer-wall out-of-plane bending modes with the natural frequencies from 12.8 Hz to 13.2 Hz. The secondary truss is active in a large number of modes.

Random response analyses were performed on the baseline configuration for the three conditions discussed in the previous section.

The RMS pointing and focus errors from 0.1 Hz to 25 Hz are summarized in Table 2. The power spectral density and the cumulative energy curves for the y-pointing error with locked rotor condition, 2% damping and Case 1 are shown in Figs. 9 and 10 as an example.

Table 2 – RMS pointing and focus errors for baseline configuration

	Case 1 – Open Locked Rotor 2% Damping	**Case 2 – Closed Locked Rotor 2% Damping**	**Case 1 – Open Locked Rotor 0.5% Damping**
	RMS Pointing Error X Direction (arcsec)		
Minimum	0.206	0.077	0.471
Maximum	0.217	0.081	0.509
Weighted Mean	0.198	0.076	0.465
	RMS Pointing Error Y Direction (arcsec)		
Minimum	0.455	0.177	0.935
Maximum	0.475	0.184	0.986
Weighted Mean	0.459	0.179	0.947
	RMS Focus Error Z Direction (mm)		
Minimum	0.205	0.077	0.371
Maximum	0.338	0.117	0.730
Weighted Mean	0.250	0.093	0.457

Table 2 shows the weighted mean RMS point errors to be 0.198 and 0.459 arcsec in the x and y-directions, respectively, and the weighted mean RMS focus error to be 0.250 mm for Case 1 (vent gates open and wind screen open) with locked rotor condition and 2% damping.

The PSD curves for the y-direction pointing error in Fig. 9 show that there are three peaks at about 5.40, 6.38, and 7.41 Hz, which match very well with the telescope fore-aft translation mode at 5.40 Hz, the secondary truss fore-aft translation and instrument platform mode at 6.83 Hz, and the secondary truss fore-aft translation mode at 7.41 Hz, respectively. Cumulative energy curves, Fig. 10, show that the secondary truss fore-aft translation mode at 7.41 Hz contributes significantly to the total error.

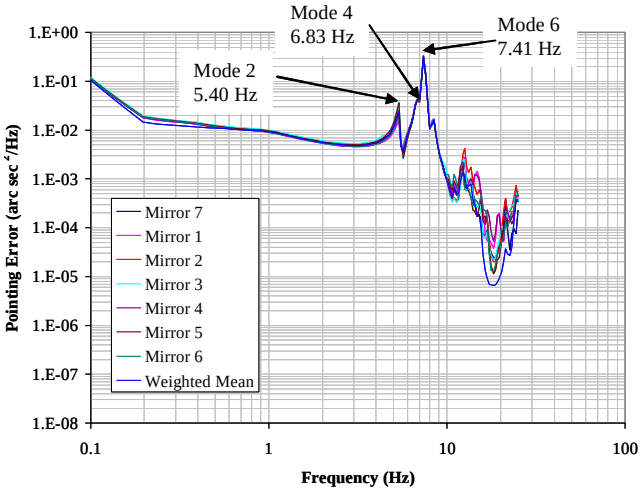

Fig. 9 – PSD of pointing error in y-direction for baseline configuration

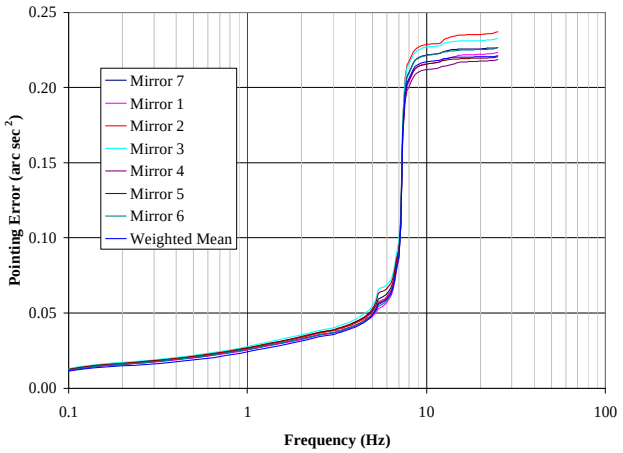

Fig. 10 – Cumulative energy of pointing error in y-direction for baseline configuration

Similar observations can be made on the PSD and cumulative energy curves for the x-direction pointing error and for the focus error. The secondary truss lateral translation and piston modes are the significant contributors to the total errors.

Therefore, for the baseline configuration, the modes of the secondary truss contribute significantly to the pointing and focus errors. Further examination of the relevant mode shapes shows that the secondary truss legs are bending in both the in-plane and out-of-plane directions and that the support brackets at the bases of the secondary truss legs are rotating (as shown in Fig. 11). Stiffening the secondary truss and bracing its support brackets should improve the optical performance of the telescope. Several secondary truss stiffening options were analyzed. The details and the results are discussed in the next section.

6.2 Results for Secondary Truss Stiffening Options

The results of baseline configuration show that the main contributor to the pointing error is the motion of the secondary mirror. Examination of the relevant mode shapes shows that the rotational flexibility of the secondary truss support bracket and the bending flexibility (in plane and out of plane) of the secondary truss may be adding to the motion of the secondary mirror.

A series of random response analyses were performed to examine the effect of the following secondary truss stiffening options:

- Option 1 – Braced Secondary Truss Support Bracket. Two 5-in. diameter Schedule 40 pipes, as shown in Fig. 12, were added to stiffen the secondary truss support bracket against rotation.
- Option 2 – Option 1 and Braced Upper Truss. In addition to the braced secondary truss support bracket, diagonal and horizontal braces were added to the upper portion of the secondary truss as shown in Fig. 12. These braces were given the properties of a rectangular hollow steel tube 20 in. x 4 in. x 0.5 in. Distributed wind loads were applied to these braces.
- Option 3 – Option 1 and Upper Truss with Double Wall Thickness. In addition to the braced secondary truss support bracket, the areas and moments of inertia of the elements of the upper truss legs were doubled to approximate doubling of the wall thicknesses.
- Option 4 – Option 2 and Secondary Truss Legs with 50% Deeper Section. In addition to the braced secondary truss support bracket and the braced upper truss, the depths of the elements of the secondary truss legs were increased by a factor of 1.5. The distributed wind loads were also increased to account for the increased depth.

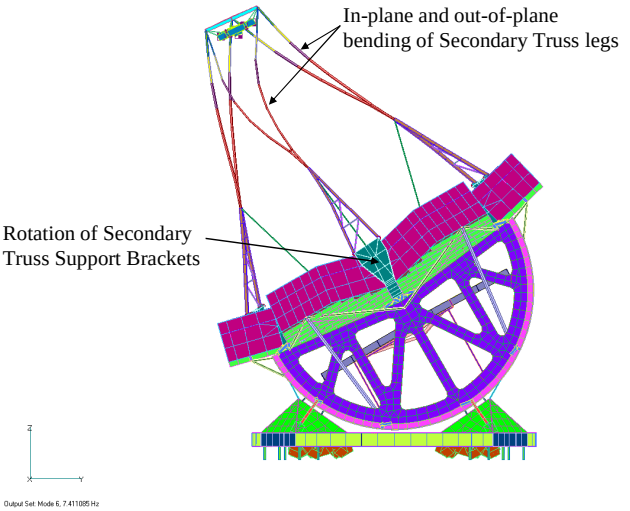

Fig. 11 – Mode 6 (7.41 Hz) for baseline configuration with locked-rotor condition

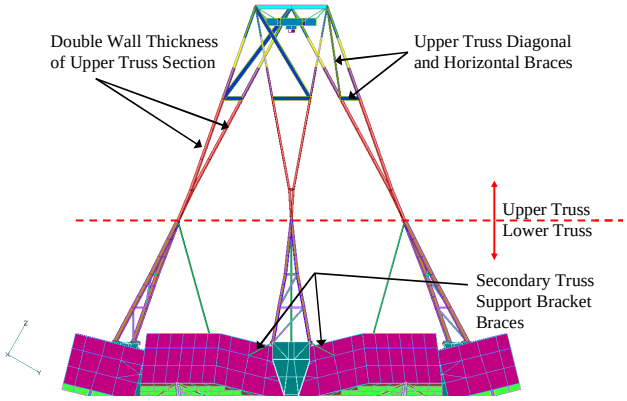

Fig. 12 – Secondary truss stiffening options

For all the above analyses, the locked rotor condition with 2% damping and Case 1 (vent gates open and wind screen open) was used. The RMS pointing and focus errors from 0.1 Hz to 25 Hz are summarized in Table 3 together with those of the baseline configuration.

Table 3 shows that each of the stiffening options significantly reduces the pointing errors. Based on the above results, a configuration that includes addition of braces to stiffen the secondary truss support brackets (Option 1), addition of diagonal and horizontal braces to the upper truss (Option 2), and the increased thickness of upper truss (Option 3), was recommended.

Table 3 – RMS pointing and focus errors for secondary truss stiffening options

	Baseline Configuration	Option 1	Option 2	Option 3	Option 4
	RMS Pointing Error X Direction (arcsec)				
Minimum	0.206	0.159	0.136	0.133	0.142
Maximum	0.217	0.189	0.146	0.155	0.156
Weighted Mean	0.198	0.153	0.123	0.122	0.128
	RMS Pointing Error Y Direction (arcsec)				
Minimum	0.455	0.364	0.274	0.295	0.283
Maximum	0.475	0.384	0.294	0.312	0.307
Weighted Mean	0.459	0.368	0.277	0.297	0.289
	RMS Focus Error Z Direction (mm)				
Minimum	0.205	0.197	0.143	0.162	0.140
Maximum	0.338	0.359	0.264	0.300	0.263
Weighted Mean	0.250	0.237	0.163	0.208	0.155

6.3 Results for Recommended Configuration

Eigenvalue analysis and random response analyses for the recommended configuration were performed. Table 4 lists resulting natural frequencies and mode shapes with locked-rotor condition.

Table 4 – Natural frequencies and mode shapes of recommended configuration

Mode	Frequency (Hz)	Mode Shape
1	4.40	Lateral Translation
2	5.35	Fore-Aft Translation
3	5.57	Azimuth Rotation
4	6.85	Secondary Truss Fore-Aft + Instrument Platform
5	7.31	Secondary Truss Lateral
6	7.75	Secondary Truss Fore-Aft
7	8.41	Secondary Truss 2:00 to 7:00
8	8.51	Secondary Truss 5:00 to 11:00
9	9.37	Secondary Truss Torsion

Random response analyses were performed on the baseline configuration for the same three conditions used on the baseline configuration. The RMS pointing and focus errors from 0.1 Hz to 25 Hz are summarized in Table 5. The power spectral density and the cumulative energy curves for the y-pointing error with locked rotor condition, 2% damping and Case 1 are shown in Figs. 13 and 14 as an example.

Comparing Table 5 to Table 2 shows that the pointing and focus errors for recommended configuration are about 0.5 times those for the baseline configuration. As shown in Figs. 9, 10, 13, and 14, the peaks in the PSD and cumulative energy curves from the secondary truss modes have been significantly reduced as the results of the secondary truss stiffening.

Table 5 – RMS pointing and focus errors for recommended configuration

	Case 1 – Open Locked Rotor 2% Damping	Case 2 – Closed Locked Rotor 2% Damping	Case 1 – Open Locked Rotor 0.5% Damping
	RMS Pointing Error X Direction (arcsec)		
Minimum	0.106	0.036	0.209
Maximum	0.117	0.040	0.236
Weighted Mean	0.091	0.035	0.184
	RMS Pointing Error Y Direction (arcsec)		
Minimum	0.196	0.077	0.355
Maximum	0.211	0.083	0.394
Weighted Mean	0.195	0.078	0.364
	RMS Focus Error Z Direction (mm)		
Minimum	0.121	0.046	0.223
Maximum	0.230	0.074	0.431
Weighted Mean	0.143	0.052	0.271

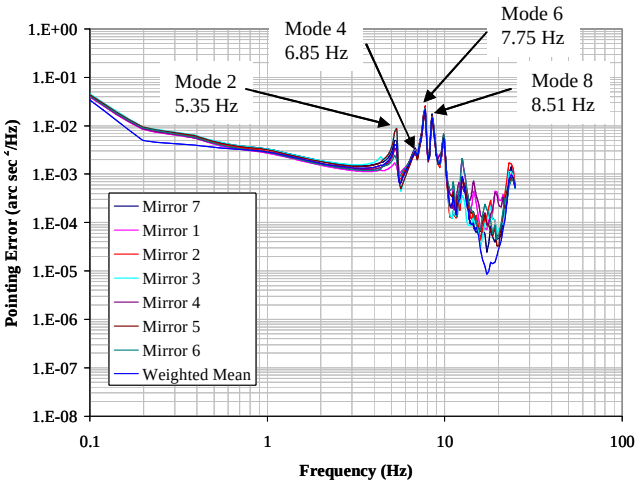

Fig. 13 – PSD of pointing error in y-direction for recommended configuration

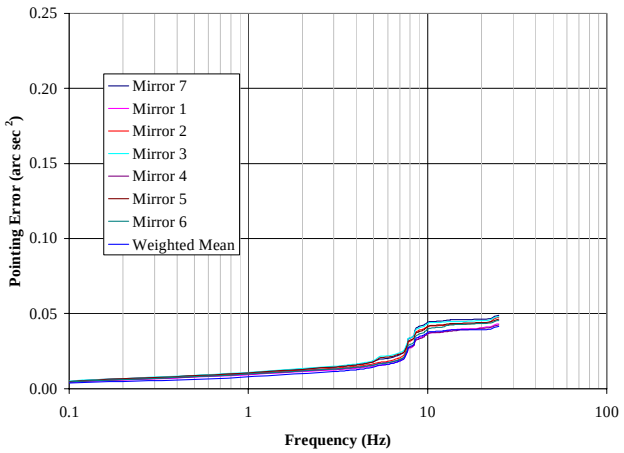

Fig. 14 – Cumulative energy of pointing error in y-direction for recommended configuration

Effect of Closed and Open Vent Gates and Wind Screen

The wind loads on the telescope structure for Case 2 (vent gates closed and wind screen closed) are significantly less than those for Case 1 (vent gates open and wind screen open). As shown in Table 5, the RMS pointing and focus errors for Case 2 are about 0.4 times those for Case 1.

Effect of Damping

Damping has a significant effect on the magnitude of the structural response to dynamic loadings. The damping for the GMT structure is expected to range from 0.5% to 2% of critical damping. Table 5 shows the RMS pointing error in the y-direction for 0.5% damping to be about 1.9 times that for 2% damping.

6.4 Results of Other Sensitivity Analyses

Additional sensitivity analyses were performed to investigate the effects of the correlation of the forces on the M2 mirrors and the effects of the different methods of applying wind loads on the M1 mirrors. The results of these sensitivity analyses are summarized in this section.

Correlated and Uncorrelated Forces on M2

Random response analyses were performed using the baseline configuration with correlated and uncorrelated forces on the M2 mirrors. The wind loads on the seven M2 mirrors were applied as concentrated forces at the C.G. of the seven mirror-cell assemblies. These forces can be considered fully correlated or uncorrelated. The correlated forces will impose a larger combined force on the secondary support structure but will not impose the additional resultant moment that may occur due to the difference in forces among the seven M2 mirrors. In this comparison, the locked rotor condition with 2% damping and Case 1 (vent gates open and wind screen open) was used.

The results show that there is only a small difference in RMS pointing errors in the x and y-directions for the correlated and uncorrelated cases. The RMS focus error is slightly larger for the correlated case. Therefore, the difference between the correlated and uncorrelated cases is not significant relative to other factors that contribute to the pointing errors. The correlated case was chosen to be the default case for all other analyses since it gives slightly more conservative results.

Effect of M1 Mirror Loading Method

Two methods of loading the M1 mirrors were examined: Method 1 – force and moment method, and Method 2 – pressure zone method. These methods are described in the dynamic wind load section. Random response analyses were performed using one of the secondary truss stiffening options (Option 1) and locked rotor condition with 2% damping and Case 1 (vent gates open and wind screen open).

These results show that there is only a small difference in RMS pointing errors in the x and y-directions for the two methods in part due to the larger effect of M2 mirror which remains unchanged. The RMS focus error is slightly larger for the force and moment method. Therefore, the difference between the two methods of M1 mirror loading is not significant relative to other factors that contribute to the pointing errors. The force and moment method was chosen to be the default case for all other analyses, since it gives slightly more conservative results.

7. DISCUSSION AND CONCLUSIONS

In this study, the wind data recorded at Gemini South was used because this test contains one of the most comprehensive pressure and velocity measurements on an actual telescope structure. The time history records and the power spectral density curves are available for a variety of cases. The dynamic wind loads on the GMT structure were calculated by adjusting and adapting the pressure and velocity measurements at Gemini South.

However, if more accurate results are needed, there are some limitations in using this approach:

- The shape of the Gemini enclosure is different from the carousel-type enclosure currently envisioned for GMT. The arrangements of the shutters and vents for the two enclosures are not the same. The wind flow around and through the two enclosures will be different.
- The Gemini South Telescope has a single 8-m optical mirror and the GMT will have seven 8.4-m mirrors. The two telescope structures and secondary support trusses do not share a lot of similarities. The wind flow around the two telescope structures are not the same.
- Almost all the wind measurements at Gemini South were performed with the wind screen open. This may not be the typical observation mode. By using the wind measurement with the wind screen open, the wind loads calculated for the secondary mirrors, the secondary support structure, and secondary truss may be too conservative.

For the preliminary and final design phases, wind tunnel tests or computational fluid dynamic analyses for the GMT enclosure and telescope structure are needed to better define the wind disturbance on the GMT structure.

Damping has a significant effect on the dynamic response. Further investigation is needed to determine the optimal level of damping to minimize the pointing errors without adversely affects other aspects of the telescope performance.

Additional design effort on the top end of the telescope is needed since it still contributes most to the pointing errors.

Wind vibration analyses were performed on the baseline configuration of the GMT structure to determine order of magnitude pointing and focus errors resulting from the dynamic response of the telescope structure to wind disturbances and to identify possible changes to the structure to reduce the optical errors. Wind pressure and velocity data recorded at the 8-m Gemini South Telescope were used to estimate the dynamic wind load on the GMT structure. Random response

analyses were performed on a finite element model of the telescope structure to determine the structural response to dynamic wind loading and the resulting optical errors. Several areas that significantly contribute to the optical errors were identified using the spectral response curves and the mode shapes. Modifications to these areas were developed and analyzed to determine their effects on the optical performance, and an improved design was developed for the next phase of the design.

ACKNOWLEDGEMENTS

Wind pressure and velocity measurements used in this research were made at the Gemini Observatory, which is operated by the Association of Universities for Research in Astronomy, Inc., under a cooperative agreement with the NSF on behalf of the Gemini partnership: the National Science Foundation (United States), the Particle Physics and Astronomy Research Council (United Kingdom), the National Research Council (Canada), CONICYT (Chile), the Australian Research Council (Australia), CNPq (Brazil) and CONICET (Argentina).

REFERENCES

1. Gunnels, S., Davison, W., Cuerden, B., and Hertz, E., "The Giant Magellan Telescope (GMT) Structure," *Astronomical Structures and Mechanisms Technology*, J. Antebi, and D. Lemke, Eds., Proceedings of SPIE Vol. 5495, Glasgow, Scotland, UK, 21-22 June 2004, p. 168-179.
2. Giant Magellan Telescope, Carnegie Observatories, http://www.gmto.org/imagegallery
3. Cho, M., Stepp, L., Angeli, G., and Smith, D., " Wind Loading of Large Telescopes," *Large Ground-based Telescopes*, J. Oschmann and L. Stepp, Eds., Proceedings of SPIE Vol. 4837, Waikoloa, Hawaii, USA, 22-26 August 2002, p. 352-367.
4. Smith, D., http://www.aura-nio.noao.edu/studies/smith0208/index.html
5. National Research Council of Canada (NRC-CNRC), *User's Guide to National Building Code 1995 Structural Commentaries (Part 4)*, 1st edition, 1996.
6. Johns, M., "Optical Sensitivity Equations for use in the Dynamical Response Analysis for the Giant Magellan Telescope", Giant Magellan Telescope Internal Document, 10 June 2005.